ACS APPLIED MATERIALS & INTERFACES

Research Article

www.acsami.org

Porous Carbon Protected Magnetite and Silver Hybrid Nanoparticles: Morphological Control, Recyclable Catalysts, and Multicolor Cell Imaging

Hui Wang,[†] Jing Shen,[†] Yingyu Li,[†] Zengyan Wei,[‡] Guixin Cao,[§] Zheng Gai,[§] Kunlun Hong,[§] Probal Banerjee,[†] and Shuiqin Zhou*[,†]

[†]Department of Chemistry of The College of Staten Island and The Graduate Center, The City University of New York, Staten Island, New York 10314, United States

[‡]Department of Chemistry and Biochemistry, Hunter College, The City University of New York, New York, New York 10065, United States

[§]Center for Nanophase Materials Sciences, Oak Ridge National Laboratory, Oak Ridge, Tennessee 37831, United States

Supporting Information

ABSTRACT: A simple and facile synthetic strategy is developed to prepare a new class of multifunctional hybrid nanoparticles (NPs) that can integrate a magnetic core with silver nanocrystals embedded in porous carbon shell. The method involves a one-step solvothermal synthesis of Fe_3O_4@C template NPs with Fe_3O_4nanocrystals in the core protected by a porous carbon shell, followed by loading and in situ reduction of silver ions in the carbon shell in water at room temperature. The core−satellite and dumbbell-like nanostructures of the resulted Fe_3O_4@C−Ag hybrid NPs can be readily controlled by loading amount of silver ions. The hybrid NPs can efficiently catalyze the reduction reaction of organic dyes in water. The easy magnetic separation and high stability of the catalytically active silver nanocrystals embedded in the carbon shell enable the hybrid NPs to be recycled for reuse as catalysts. The hybrid NPs can also overcome cellular barriers to enter the intracellular region and light up the mouse melanoma B16F10 cells in multicolor modal, with no cytotoxicity. Such porous carbon protected Fe_3O_4@C−Ag hybrid NPs with controllable nanostructures and a combination of magnetic and noble metallic components have great potential for a broad range of applications in the catalytic industry and biomedical field.

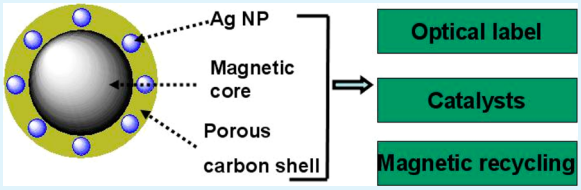

KEYWORDS: *magnetite−silver hybrid nanoparticles, porous carbon shell, core−satellite and dumbbell-like, catalytic activity, cell imaging*

1. INTRODUCTION

With the development of nanoscience and nanotechnology, the synthesis of multi-component hybrid nanostructures by combining different component nanoparticles (NPs) into a single object has gained significant momentum in recent years.[1−12] Such multi-component NPs can realize the combination of different functionalities from the unique optical, electronic, catalytic, and magnetic properties of the individual component, therefore, providing potential applications in many fields.[7,8,13−19] For example, composite NPs containing both iron oxide and noble metal nanocrystals can not only serve as imaging agent for magnetic resonance and optical imaging[18,19] but also allow biomolecules to be tagged and magnetically separated.[19−23] In addition, these hybrid NPs can be used as recyclable catalyst for the reduction and degradation of organic pollutant.[16,24−26] However, because of their high surface energies, these hybrid NPs tend to coagulate and/or change shape in catalytic reactions and eventually lose their initial activity and selectivity. Moreover, the naked iron oxide and noble metal NPs could be toxic to cells and may induce oxidative stress processes in the body.[26−30] It remains an important challenge to improve the stability and recyclability of these hybrid NPs as catalysts and the biocompatibility of these hybrid NPs as biomedical reagent.

The surface coating of these NPs can significantly improve their colloidal stability and biocompatibility.[31,32] Recently, it has been reported that noble metal or iron oxide NPs can be greatly stabilized against aggregation and coalescence by the surface coating with silica shell.[33−36] However, these inorganic coatings will make it difficult for the reactant molecules to reach the encapsulated active NPs because of the dense structure of the outer layer, limiting the use of these core−shell structured NPs as catalysts. The encapsulation with porous shells not only makes the catalytically active metal NPs accessible but also keeps them stable even under harsh reaction conditions.[25,37−42] Unfortunately, the synthesis of these designed structures involves multiple steps and sacrificial templates, likely rendering the catalysts too expensive for widespread industrial use.

Received: May 30, 2013
Accepted: September 3, 2013
Published: September 3, 2013

Furthermore, the multifunctional hybrid NPs involving multiple components were usually prepared in organic solvents by redox reaction or at high temperature by thermal decomposition.[43−46] It is necessary to transfer these acquired NPs from organic phase to aqueous phase through ligand exchange or micelle systems for potential use in biomedicine. In addition, few methods have been developed for systematic control over the morphology and nanostructure of the resulted hybrid NPs protected by porous shell, making it difficult to control the mass transfer of the reactants and products in catalytic reactions. A worthwhile synthetic challenge, therefore, is to develop a general and facile synthetic approach to fabricate multifunctional hybrid NPs with good stability in aqueous phase and controllable hybrid nanostructures within the porous shells for both catalytic and biomedical applications.

We describe herein a convenient and simple strategy to prepare the magnetite−silver hybrid NPs with good stability in water and controllable nanostructures for multifunctional applications. The strategy to prepare the multifunctional hybrid NPs involves the first one-step solvothermal synthesis of the porous carbon (C) shell protected magnetic iron oxide (Fe_3O_4) nanocrystals (Fe_3O_4@C) as template, followed by the adsorption and in situ reduction of silver ions (Ag^+) in the carbon shell under the assistance of $NaBH_4$ in aqueous phase. Figure 1 schematically outlines the simple and straightforward

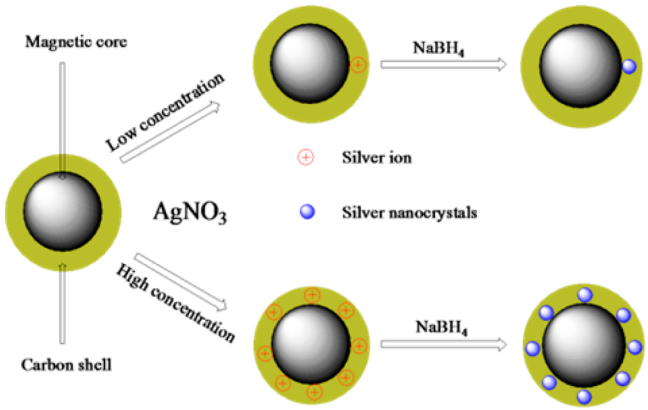

Figure 1. Schematic illustration of the nanostructure control for the Fe_3O_4@C−Ag hybrid NPs with core−satellite and dumbbell-like morphology by a simple concentration change of Ag^+ ions in reaction medium.

procedure to synthesize the carbon shell protected magnetic−silver hybrid NPs (Fe_3O_4@C−Ag) with controllable nanostructures. Compared to the reported Fe_3O_4−Ag hybrid NPs,[14−17] which are typically synthesized by multiple steps in organic solvents with capping agents/dispersing surfactants and require complicated transferring procedures to be dispersed into aqueous phase, our Fe_3O_4@C−Ag hybrid NPs has several advantages from both synthetic and application point of view. First, the surface hydroxyl and carboxyl groups on the porous carbon shell produced from the solvothermal synthesis of the Fe_3O_4@C template NPs can promote the adsorption and stabilization of Ag^+ ions in the shell from aqueous solution; thus, the Ag NPs can be in situ formed in the hydrophilic carbon shell, and the resulting hybrid NPs can disperse very well in water with no need of additional dispersing agents. Second, different morphologies including core−satellite and dumbbell-like nanostructures of the hybrid NPs can be readily controlled by a simple change of the initial concentration of Ag^+ ions in the reaction medium. Third, for catalytic application, our hybrid NPs with the noble metallic Ag nanocrystals in the porous carbon shell allow the reactant molecules to reach the surface of catalyst (Ag nanocrystals) to participate in reactions, but the porous shells can still act as physical barriers to prevent the aggregation of the catalyst particles. Meanwhile, the magnetically separable Fe_3O_4@C−Ag hybrid NPs can be redispersed quickly in water, thus providing an easy recyclability as catalysts. Fourth, for biological applications, the hydrophilic porous carbon shell protected hybrid NPs can serve as potential drug carriers to facilitate simultaneous imaging diagnosis and drug therapy. Therefore, the resulted Fe_3O_4@C−Ag hybrid NPs that can combine the strong fluorescence and catalytic activity of Ag nanocrystals, the magnetic responsive property of Fe_3O_4 core, and the hydrophilic carbon shell should find broad applications in both the catalytic industry and biomedical field.

2. EXPERIMENTAL SECTION

2.1. Materials. All chemicals were purchased from Aldrich. Ferrocene ($Fe(C_5H_5)_2$, ≥98%), hydrogen peroxide (H_2O_2, 30%), acetone (C_3H_6O), silver nitrate ($AgNO_3$), sodium borohydride ($NaBH_4$), and Rhodamine B were used as received without further purification. The water used in all experiments was of Millipore Milli-Q grade.

2.2. Synthesis of Fe_3O_4@C Core−Shell Template NPs. The synthesis of Fe_3O_4@C NPs follows the reported method with some modification.[47,48] In brief, 0.60 g of ferrocene was added into 60 mL of acetone. After intense sonication for 15 min, 3.0 mL of H_2O_2 (30%) was slowly added into the above solution with a gentle shaking. The resulted solution was transferred to a Teflon-lined stainless autoclave with a total volume of 100 mL. After sealing it, the autoclave was heated to and maintained at 200 °C for 24 h. The autoclave was then cooled naturally to room temperature. The products from the autoclave were washed with acetone three times and dried.

2.3. Synthesis of Fe_3O_4@C−Ag Hybrid NPs with Different Nanostructures. The reaction conditions, such as initial concentration of Ag^+ ions, reaction temperature, and time, can be used to control the nanostructures of the hybrid NPs. A typical method for synthesis of dumbbell-like Fe_3O_4@C−Ag hybrid NPs is as follow: 0.01 g of Fe_3O_4@C template NPs was dispersed into 20 mL of distilled water to form a suspension with a concentration of 500 mg/L. Then, 5 mL of such a Fe_3O_4@C NP suspension and 0.5 mL of $AgNO_3$ aqueous solution of 0.01 mol/L were transferred to a vial. After being vigorously stirred for 15 min, 5 mL of aqueous solution of $NaBH_4$ (0.01 mmol/L) was added, followed by the addition of distilled water to ensure a total solution volume of 20 mL. Then, the resulted mixture solution was heated to and maintained at a temperature of 30 °C under the magnetic stirring condition. After 15 min, the reaction system was cooled naturally to room temperature. The products from the vial were magnetized for 10 min by a magnet of 0.30 T, and the supernatant was discarded under a magnetic field. The precipitates were then washed three times with distilled water to remove those free Ag nanocrystals that were not embedded into the carbon shell. Finally, the black products were dried at room temperature. In this reaction system, the increase in reaction temperature (e.g., 60 and 90 °C) or the extension of reaction time (e.g., 30 and 60 min) can also produce the dumbbell-like hybrid NPs. In order to synthesize the core−satellite structured Fe_3O_4@C−Ag hybrid NPs, the same synthetic procedure described above can be used. However, the more concentrated $AgNO_3$ in the reaction solution and milder reaction conditions are required. Typically, 1 mL of $AgNO_3$ aqueous solution of 0.1 mol/L needs to be used to mix with the 5 mL of Fe_3O_4@C NP suspension of 500 mg/L in the initial procedure described above. The reduction reaction of Ag^+ ions needs to be maintained at 30 °C for 15 min or less.

2.4. Catalytic Activity of Fe_3O_4@C−Ag Hybrid NPs. In a typical catalytic experiment, both dye (Rhodamine B, 2×10^{-5} mol/L) and $NaBH_4$ (0.01 mol/L) aqueous solutions were freshly prepared.

dx.doi.org/10.1021/am4032532 | ACS Appl. Mater. Interfaces 2013, 5, 9446−9453

Subsequently, a 5 mL suspension (500 mg/L) of the Fe_3O_4@C−Ag hybrid NPs as catalyst was mixed with 5 mL of Rhodamine B solution, and then, 10 mL of fresh $NaBH_4$ solution was rapidly injected into this mixture while stirring. The color of the mixture was fading with the experiment proceeding, indicating a gradual reduction of the Rhodamine B dye molecules. The catalytic activity of the hybrid NPs was studied by monitoring the variation of the maximum absorbance at the wavelength of 554 nm with a UV−vis spectrometer. After the reaction was completed, the catalyst of hybrid NPs was quickly separated from the solution using a NdFeB magnet, rinsed with water, and re-dispersed into 5 mL of distilled water. The recovered catalyst was then re-added into a mixture of new reactants to initiate another reaction cycle. The same procedure was performed in the additional 8 cycles.

2.5. Internalization of Hybrid NPs into Mouse Melanoma Cells B16F10. Round glass coverslips were placed in wells of a 24-well plate and treated with 0.1% poly-L-lysine in 100 mM phosphate buffered saline (PBS) for 40 min. Following the treatment, the solution was aspirated, and the wells were washed with PBS 3 times each. Next, B16F10 cells (2×10^4 cell/well) were plated on the glass coverslips at 80% confluence in DMEM containing 10% FBS and 1% penicillin−streptomycin. After 24 h, 500 μL of core−satellite structured Fe_3O_4@C−Ag hybrid NPs in serum-free DMEM (50 mg/mL) was, respectively, added to the marked wells. In a control well, 500 μL of serum-free DMEM was added. The plate was incubated at 37 °C for 2 h. The medium was then aspirated, and fresh serum-free DMEM was added to each well. Finally, the coverslips with cells were removed from the wells and mounted onto slides for confocal microscopy study.

2.6. In Vitro Cytotoxicity of the Fe_3O_4@C−Ag Hybrid NPs. The cytotoxicity of the Fe_3O_4@C−Ag hybrid NPs was evaluated on the mouse melanoma cell line B16F10. Typically, B16F10 cells were cultured in a 96 well microplate in 100 μL of medium containing about 2000 cells seeded in each well. After an overnight incubation for attaching, the medium was removed. Another 100 μL of medium containing the Fe_3O_4@C−Ag hybrid NPs in different nanostructures was, respectively, added to make the final extract concentration at 200, 150, 100, and 50 μg/mL. After incubation for 72 h, 25 μL of 3-(4,5-dimethyl-2-thiazolyl)-2,5-diphenyltetrazolium bromide (MTT) solution (5 mg/mL in PBS) was added into the wells and incubated in a humidified environment of 5 % CO_2 and 37 °C for 2 h. The medium was removed after 2 h, and 100 μL of DMSO solution was added to dissolve the formazan crystal; the plate was sealed and incubated overnight at 37 °C with gentle mixing. Three portions of the solution obtained from each well were transferred to three respective wells of a 96-well plate. Cell viability was measured using a microplate reader at 570 nm. Positive controls contained no hybrid NPs, and negative controls contained MTT. Parallel wells (in triplicate) also contained only medium (no cells) and the same concentrations of hybrid NPs.

2.7. Characterization. The UV−vis absorption spectra were obtained on a Thermo Electron Co. Helios β UV−vis spectrometer. The photoluminescence (PL) spectra of hybrid NPs in aqueous suspensions were obtained on a JOBIN YVON Co. FluoroMax-3 spectrofluorometer equipped with an xenon lamp as light source and a Hamamatsu R928P photomultiplier tube as detector, calibrated photodiode for excitation reference correction from 200 to 980 nm, and an integration time of 1 s. The pH values were measured on a METTLER TOLEDO SevenEasy pH meter. The surface area and pore volume was collected by accelerated surface area and porosimetry (ASAP 2020 M+C). The FT-IR spectrum of the hybrid NPs was recorded with a Nicolet Instrument Co. MAGNA-IR 750 Fourier transform infrared spectrometer. The content of Ag nanocrystals in the hybrid NPs was measured using inductively coupled plasma-atomic emission spectroscopy (ICP-AES) (Atomscan Advantage). The transmission electron microscopy (TEM) images were taken on a FEI TECNAI transmission electron microscope at an accelerating voltage of 120 kV. Approximately 10 μL of the hybrid NPs dispersion in water was dried on a carbon-coated copper grid for the TEM measurements. High-resolution TEM (HRTEM) images were characterized on a JEM 2100 (JEOL) transmission electron microscope at an acceleration voltage of 200 kV. Energy-dispersive X-ray (EDX) analysis was obtained with an EDAX detector installed on the same HRTEM equipment. A superconducting quantum interference device (SQUID) magnetometer (Quantum Design MPMS XL-7) was used to measure the field dependent magnetization of as-prepared hybrid NPs at room temperature and temperature dependent magnetization from 4 K up to 400 K. The B16F10 cells incorporated with hybrid NPs were imaged using a confocal laser scanning microscopy (LEICA TCS SP2 AOBSTM) equipped with a HC PL APO CS 20×0.7 DRY lens at different laser wavelengths of 405, 488, and 546 nm. The corresponding image detection channel wavelength ranges are 405−462, 493−540, and 584−688 nm, respectively. A UV (405 nm) light was used as the light source. Dynamic light scattering (DLS) measurement was performed on a standard laser light scattering spectrometer (BI-200SM) equipped with a BI-9000 AT digital time correlator (Brookhaven Instruments, Inc.) to determine the hydrodynamic radius (R_h) distributions of the hybrid NPs dispersed in water (refractive index = 1.333) at a scattering angle of 60° and temperature of 22 °C. The refractive index of particles used for the DLS measurement is 1.59. A He−Ne laser (35 mW, 633 nm) was used as the light source. All hybrid NPs dispersions were passed through Millipore Millex-HV filters with a pore size of 0.80 μm to remove dust before the DLS measurements.

3. RESULTS AND DISCUSSION

A typical preparation of the multifunctional Fe_3O_4@C−Ag hybrid NPs starts with the solvothermal synthesis of the core−shell structured Fe_3O_4@C as template, followed by the adsorption and in situ reduction of the Ag^+ ions in the carbon shell of the template NPs. The inset in Figure 2a confirms that

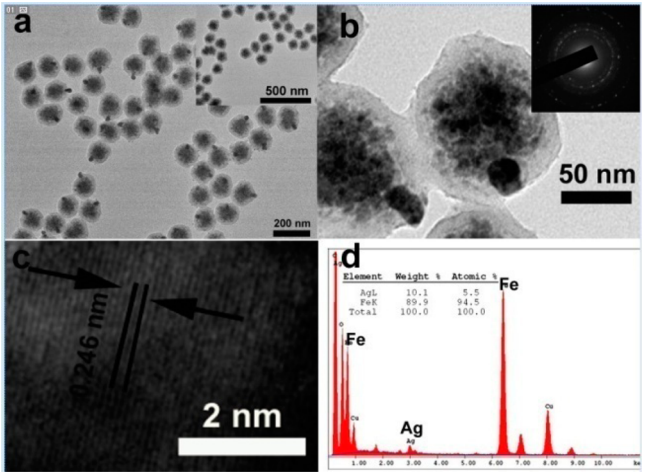

Figure 2. (a) Low and (b) high magnified TEM images of the dumbbell-like Fe_3O_4@C−Ag hybrid NPs synthesized at $[Ag^+]$ = 0.25 mM and 30 °C for 15 min. The inset in (a) is a TEM image of the Fe_3O_4@C NPs; the inset in (b) is the electron diffraction (ED) pattern of the dumbbell-like hybrid NPs. (c) The lattice fringe of Ag nanocrystals. (d) EDS and elemental ratio of a single dumbbell-like hybrid NP.

the Fe_3O_4@CNPs have a clear core−shell structure with an average size about 110 nm. Figure S1, Supporting Information, shows representative nitrogen adsorption/desorption isotherms and the corresponding pore size distribution of the Fe_3O_4@C template NPs. The BET (Brunauer−Emmett−Teller) surface area and total pore volume were determined to be 94.8 $m^2\ g^{-1}$ and 0.31 $cm^3\ g^{-1}$, respectively. The BJH (Barret−Joyner−Halenda) pore diameters calculated from the desorption branch of the isotherm show that there are large pores of different sizes in addition to the small pores of 3.9 nm. Figure S2a, Supporting

Information, shows the FT-IR spectrum of the Fe_3O_4@C template NPs dried from the aqueous solution, demonstrating characteristic broad absorptions from 1800 to 1000 cm^{-1} of disordered graphitic carbon.[49−51] The peaks at 1600 and 1412 cm^{-1} can be, respectively, assigned to the C═C stretching vibration and the skeletal/ring C−C stretching modes of polyaromatic systems in the carbon shell.[49−53] The apparent peak at about 3400 cm^{-1} can be attributed to the −OH stretching modes.[52,53] The absorption peak at 1678 cm^{-1} should be from the asymmetric carbonyl stretching of carboxylate groups conjugated with the condensed aromatic carbons,[49,53] while the symmetric carbonyl stretching modes of carboxylate are probably masked or convoluted into the main carbon peaks at 1400−1450 cm^{-1}. Considering that our Fe_3O_4@C NPs were prepared from the thermal decomposition and oxidation of ferrocene in the presence of H_2O_2 and demonstrated excellent water dispersibility, it is reasonable to conclude that the carboxylate groups are presented on the carbon shell of the Fe_3O_4@C NPs. However, the shoulder at ∼1730 cm^{-1} for −COOH groups is very weak; thus, the −COOH groups cannot be unambiguously confirmed on the NPs. Nevertheless, the carboxyl and/or hydroxyl groups should promote the adsorption and stabilization of Ag^+ ions in the porous carbon shell.[12] Therefore, the multifunctional Fe_3O_4@C−Ag hybrid NPs can be synthesized by adding a suitable amount of $AgNO_3$ into the aqueous dispersion of Fe_3O_4@C NPs under the assistance of $NaBH_4$. As shown in Figure 2b, the monodispersed Fe_3O_4@C−Ag hybrid NPs, synthesized at low concentration of Ag^+ ions ($[Ag^+]$ = 0.25 mM) and 30 °C for 15 min, contain both magnetic Fe_3O_4 core and Ag nanocrystals (25 nm) and exhibit a dumbbell-like morphology. The high-magnification TEM image in Figure 2b of a single dumbbell-like hybrid NP suggests that both the iron oxide and Ag nanocrystals are contiguous and encapsulated well within the porous carbon shell. The clear diffraction rings from the SAED pattern are indicative of the polycrystalline nature of the Fe_3O_4@C−Ag hybrid NPs. The interplanar distance (0.250 nm) of Ag nanocrystals are shown in Figure 2c, which corresponds to the (111) lattice planes of Ag. Figure 2d shows the result from the energy dispersive analysis of X-rays (EDAX) of the selected areas of a single dumbbell-like hybrid NP, which reveals the presence of Fe, Ag, O, C, and Cu elements. While the Cu is from the copper grid for TEM sample preparation, the C is from both the carbon film coated on the copper grid and the carbon shell of the hybrid NP. The Fe, O, and Ag signals result from the iron oxide and Ag nanocrystals in the hybrid NP. The ICP-AES method determines that the dumbbell-like hybrid NPs contain 5.6 wt % Ag. These data show that the Ag nanocrystals have been successfully synthesized in the porous carbon shell. In comparison with the IR spectrum of the Fe_3O_4@C template NPs (Figure S2a, Supporting Information), the encapsulation of the Ag nanocrystals in the carbon shell did not change the IR spectrum significantly (Figure S2b, Supporting Information). A small shift of the broad −OH peak might be due to the binding of the −COOH and/or −OH groups with the Ag nanocrystals.

It should be mentioned that the further extension of reaction time over 15 mins or increase in reaction temperature above 30 °C for the formation of Ag nanocrystals did not influence the nanostructure of the dumbbell-like hybrid NPs by keeping low concentration of Ag^+ ions. The TEM images shown in Figure S3, Supporting Information, indicated that the size of Ag nanocrystals basically remains unchanged with the increase in reaction time from 15 to 60 mins. It is known that the optical properties of Ag nanocrystals are strongly dependent on their sizes and shape.[54,55] The nearly identical peak position of the UV−vis absorption spectra obtained from these hybrid NPs (Figure S4, Supporting Information) further confirmed the similar size of the Ag nanocrystals in their carbon shell. These results indicate that the reduction of Ag^+ ions and growth of Ag nanocrystals could be completed within 15 mins, which demonstrates the rapid synthesis of the multifunctional Fe_3O_4@C−Ag hybrid NPs. Similarly, the increase in reaction temperature to above 30 °C has minimum effect on the Ag nanocrystal growth for the synthesis of the dumbbell-like hybrid NPs at low $[Ag^+]$ (Figures S5 and S6, Supporting Information). These results may result from the use of an exceeding amount of reductant $NaBH_4$, which can realize the rapid reduction of Ag^+ ions and growth of Ag nanocrystals in the carbon shell and consequently minimize the influence of reaction conditions on the formation of Fe_3O_4@C−Ag hybrid NPs.

On the other hand, the increase in the concentration of Ag^+ in the reaction medium can significantly change the nanostructures of the Fe_3O_4@C−Ag hybrid NPs. Figure 3a shows the typical TEM images of the Fe_3O_4@C−Ag hybrid NPs synthesized at a much higher concentration of Ag^+ ions (5 mM) and 30 °C with a reaction time of 15 min. In contrast to the dumbbell like hybrid NPs formed at low $[Ag^+]$ (Figure 2a,b), the high-magnification TEM image in Figure 3b of the single Fe_3O_4@C−Ag hybrid NP indicates that more Ag nanocrystals could be in situ formed in the porous carbon shell at high $[Ag^+]$. The Ag nanocrystals are well encapsulated within the porous carbon shell, demonstrating an obvious core−satellite structure. In order to further identify the location of Ag nanocrystals, the typical HRTEM image of the carbon shell of the core−satellite structured hybrid NPs was shown in Figure 3c. Clearly, the Ag nanocrystals with different size from about 6 to 20 nm can be found in the porous carbon shell. Figure 3d shows the EDAX result of the selected areas of a single core−satellite hybrid NP, which reveals that the hybrid

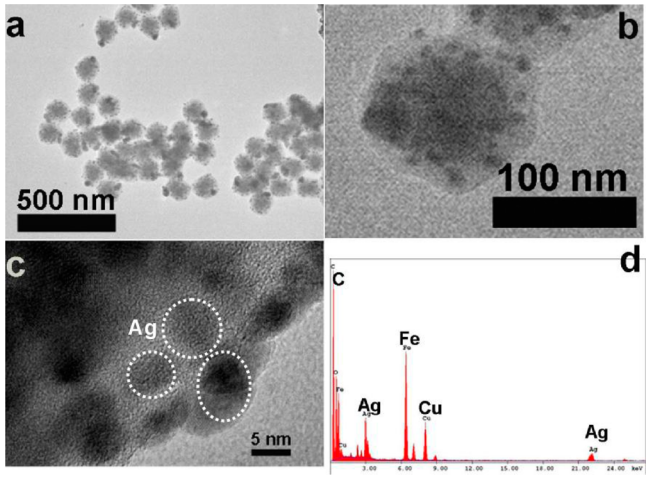

Figure 3. (a) Low and (b) high magnification TEM images of the core−satellite structured Fe_3O_4@C−Ag hybrid NPs synthesized at $[Ag^+]$ = 5 mM and 30 °C with a reaction time of 15 mins. (c) HRTEM image of the carbon shell of the core−satellite structured hybrid NP. (d) EDS and elemental ratios of a single core−satellite structured hybrid NP.

dx.doi.org/10.1021/am4032532 | ACS Appl. Mater. Interfaces 2013, 5, 9446−9453

NPs casted on the carbon film coated copper grid contain Fe, Ag, O, C, and Cu elements. The ICP-AES method determines that the core−satellite hybrid NPs contain 31.2 wt % Ag. The high Ag/Fe atomic ratio also indicates that the core−satellite structured hybrid NPs contain more Ag nanocrystals, which should be more efficient as noble metallic catalysts and optical imaging agents.

The magnetic hysteresis loop (Figure 4) of the core−satellite structured Fe_3O_4@C−Ag hybrid NPs was measured at 300 K in

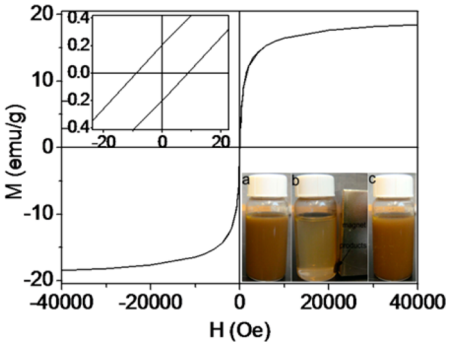

Figure 4. Hysteresis loop measured at room temperature for the core−satellite structured hybrid NPs. The left inset shows the respective expanded plots for the field between −20 and 20 Oe. The right inset shows the photographs of the hybrid NPs dispersed in water (a) without magnetic field, (b) with magnetic field for 1 min, and (c) after the removal of magnetic field.

an applied magnetic field of up to 40 000 Oe. An expanded plot in the inset for field strengths between −20 and 20 Oe reveals a weakly ferromagnetic nature of the hybrid NPs at room temperature. The temperature dependence of zero-field-cooled (ZFC) and field-cooled (FC) magnetization for the as-prepared hybrid NPs is presented in Figure S7, Supporting Information. ZFC and FC curves separate from each other from 5 to 325 K, and no transition from ferromagnetism to superparamagnetism can be observed, which further confirms the weak ferromagnetism of the hybrid NPs at room temperature.[56] The core−satellite structured hybrid NPs exhibited a saturation magnetization (Ms) of 18.43 emu/g. When the aqueous dispersion of the hybrid NPs is subjected to a magnetic field (0.30 T),the NPs can be attracted toward the magnet side within minutes, as shown in the inset of Figure 4a,b. Slight agitation will bring the hybrid NPs back into the original uniform dispersion in water after the magnetic field was removed (Figure 4c). The quick magnetic response and redispersibility of the newly designed hybrid NPs in water are very important for their future applications in bioseparation, storage, and magnetic targeting drug delivery, because the porous carbon shell can also serve as carriers for drug and other functional molecules. The good dispersibility of the Fe_3O_4@C−Ag hybrid NPs in water was further confirmed by the dynamic light scattering measurement result (Figure S8, Supporting Information). The narrow size distribution with an average hydrodynamic diameter of 120 nm demonstrates that the hybrid NPs are stable in water and do not form aggregates. The exceptional colloidal stability of the Fe_3O_4@C−Ag hybrid NPs in aqueous media is attributed to the $-COO^-$ and −OH groups presented on the surface of porous carbon shell.

Concerning the prospective catalytic applications of Ag nanocrystals for many chemical reactions, the catalytic activity of the Fe_3O_4@C−Ag hybrid NPs were evaluated with organic dye Rhodamine B as a model.[57] In the absence of the hybrid NPs, the reduction of Rhodamine B did not proceed at room temperature even with a large excess of reducing agent $NaBH_4$. When a small amount of hybrid NPs was introduced into the solution with a final concentration of 0.125 mg/mL, the absorption at 554 nm gradually decreased, indicating the successful reduction of Rhodamine B. By using the calibration curve obtained from the maximum absorption intensity of the standard Rhodamine B solutions, the percentage of reduced Rhodamine B using the Fe_3O_4@C−Ag hybrid NPs as catalyst could be calculated $(=(C_0 - C_t)/C_0 \times 100$ with C_0 and C_t representing the concentrations of the dye at initial time and specific reaction time t). Figure 5a demonstrates the percentage of reduced Rhodamine B at different times after the dye solution is mixed with hybrid NPs, which reveals that the first 10 minutes have a pronounced effect on the reduction of Rhodamine B. The further increase in reduction time has a negligible effect on the reduction of Rhodamine B. The fast diffusion of reactant molecules through the large pores of the carbon shell is believed to be responsible for the fast reduction of Rhodamine B. In addition, it can be seen that more Rhodamine B molecules can be reduced by the core−satellite structured hybrid NPs than the dumbbell-like hybrid NPs at the same concentration of NPs, which should be attributed to the higher content of Ag nanocrystals in the core−satellite structured hybrid NPs. The rate constants of the Rhodamine B reduction reaction were determined to be 0.20 and 0.14 min^{-1} for the core−satellite and dumbbell-like hybrid NPs, respectively, which are much higher than the rate constant of

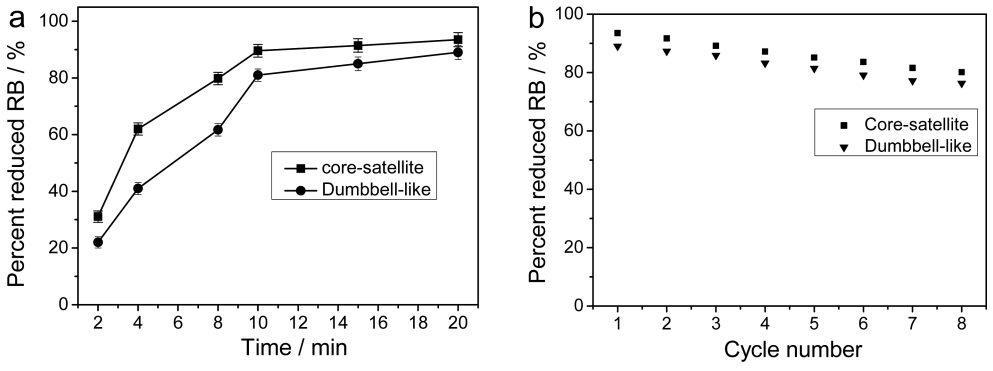

Figure 5. Percentage of reduced Rhodamine B (a) at different times after mixing the dye solution with the two different structured NPs of the same concentration and (b) at a reduction reaction time of 20 min after different recycle uses of hybrid NPs.

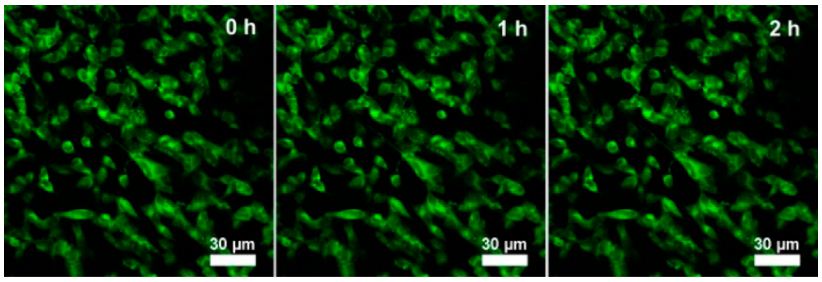

Figure 6. Laser scanning confocal microscopy images of B16F10 cells incubated with the core−satellite structured hybrid NPs under different excitation times. Excitation wavelength = 405 nm.

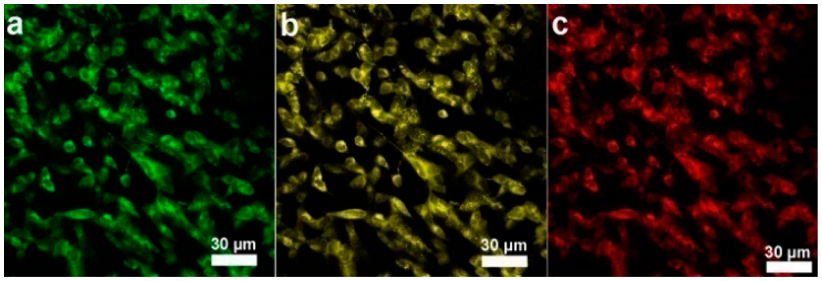

Figure 7. Laser scanning confocal images of B16F10 cells incubated with the core−satellite structured Fe_3O_4@C−Ag hybrid NPs under different excitation wavelengths: (a) 405 nm; (b) 488 nm; (c) 546 nm.

0.047 min^{-1} of the same reaction for free Ag NPs of similar size (21 nm).[58] The ratio of rate constant k over the total mass m of the used catalyst, $\kappa = k/m$, facilitates the comparison of catalytic activity.[59] For the Rhodamine B reduction reaction, the catalytic activity index κ of the Ag−Fe_3O_4 composite NPs containing about 26 wt % Ag core was estimated to be 0.53 s^{-1} g^{-1}.[60] In contrast, our Fe_3O_4@C−Ag hybrid NPs have higher activity index with κ = 1.4 and 0.93 s^{-1} g^{-1}, respectively, for the core−satellite (31 wt % Ag) and dumbbell-like (5.6 wt % Ag) structured hybrid NPs, which should be benefited from the porous carbon substrate in the catalytic reduction. It has been reported that the Ag NPs doped in porous carbon sphere exhibited much higher catalytic activity toward the reduction of 4-nitrophenol by $NaBH_4$ in comparison with the Ag NPs supported on other substrates like halloysite nanotubes or polymer spheres.[59,61−63] Because carbon is relatively electrically conductive, the authors believed that the carbon substrate takes an active role during the growing process of Ag NPs, and thus, metal−carbon interfaces also contribute an active role to the catalytic reaction. The magnetic Fe_3O_4 core enables the recollection of the hybrid NPs for reuse as catalysts. The UV−vis absorption spectrum and morphology of the hybrid NPs remain nearly unchanged after the use in catalytic reactions, demonstrating the excellent stabilization effect of the porous carbon shells on the embedded Ag nanocrystals. Figure 5b shows the percentage of reduced Rhodamine B after a successive reuse of the hybrid NPs for eight cycles. The catalytic ability of the hybrid NPs for the reduction of Rhodamine B drops slightly after each cycle, which indicates that a very small amount of Ag nanocrystals could be lost during the recycling process of magnetic separation, washing, and redispersion. Interestingly, the hybrid NPs demonstrate more stable catalytic activity after five recycle uses, possibly because the loss of a small amount of Ag nanocrystals mainly occurred at the exterior surface of the carbon shell in the initial several cycles. Overall, the porous carbon protected Ag nanocrystal catalysts in the shell of hybrid NPs is very durable.

The Ag nanocrystals embedded in the carbon shell of the Fe_3O_4@C−Ag hybrid NPs also demonstrated strong fluorescence. Figure S9a, Supporting Information, shows a comparison of the PL spectra from water, Fe_3O_4@C template NPs, and the two different structured Fe_3O_4@C−Ag hybrid NPs. The peak at lower wavelength centered at about 440 nm should be attributed to the Raman scattering from water. Clearly, the template Fe_3O_4@C NPs exhibits PL emissions in a broad wavelength range. Compared to the spectrum of the Ag-free Fe_3O_4@C template NPs, both the spectra of the core−satellite and dumbbell-like Fe_3O_4@C−Ag hybrid NPs demonstrate a broad intensive emission peak at wavelength centered at about 515 nm, which should be attributed to the strong fluorescence of the Ag nanocrystals embedded in the carbon shell. The fluorescence of noble metal NPs originates from the radiative recombination of sp-band electrons and d-band holes, which could be enhanced by 4−6 orders of magnitude due to the surface plasmons of nanocrystals or rough metal surfaces.[64] It is believed that the emissions of Ag nanocrystals are due to small Ag cluster, predominantly Ag_2 supported by the readily detectable NPs.[65] In our hybrid NPs, the Ag nanocrystals were in situ formed in the porous carbon shell, which could be stabilized by the −COOH and −OH groups on the carbon surface. Thus, the hybrid NPs should demonstrate very stable PL properties. As shown in Figure S9b, Supporting Information, negligible changes of the fluorescence intensity can be observed after a 2 h continuous excitation using a fluorescence spectrophotometer. The results indicate that the Ag nanocrystals protected by a porous carbon shell in both core−satellite and dumbbell-like hybrid NPs show excellent stability against photobleaching.

After confirming the strong fluorescence of the Fe_3O_4@C−Ag hybrid NPs, the core−satellite structured hybrid NPs were selected as an optical marker to evaluate their cellular imaging function. The mouse melanoma cells B16F10 were selected as model cells. As shown in the laser scanning confocal images in Figure 6, under the irradiation of the laser with a wavelength of

405 nm, the Ag nanocrystals encapsulated in the porous carbon shell produced a bright fluorescence and, thus, can light up the B16F10 cells. The Z-scanning confocal fluorescence images of single B16F10 cell after incubation with the hybrid NPs (Figure S10, Supporting Information) confirm that the hybrid NPs can overcome the cellular barriers to enter the intracellular region. In order to study the photostability of the hybrid NPs as optical marker, the confocal images of the B16F10 cells incubated with the core−satellite structured hybrid NPs were taken under different excitation times. Figure 6 shows that no obvious fluorescent intensity change can be observed on the cell images with the prolonged irradiation time from 0 to 2 h, providing a possibility for a long term cellular imaging application. In addition, the core−satellite structured hybrid NPs can be used for multicolor fluorescent imaging for cells. Figure 7 clearly demonstrates that the B16F10 cells can be lightened up by the incubated hybrid NPs after irradiation with a laser at different wavelengths. This phenomenon may originate from the synergy of different sizes of the fluorescent Ag nanocrystals embedded in the carbon shells of the hybrid NPs.[51,64−67] All these results suggest that the core−satellite structured Fe_3O_4@C−Ag hybrid NPs could be a good candidate as an optical marker for fluorescent bioimaging.

For future biological applications such as optical bioimaging agents and drug delivery vehicles, materials should be noncytotoxic or have low cytotoxicity. As shown in Figure 6, no signs of morphological damage to the cells were observed upon treatment with the Fe_3O_4@C−Ag hybrid NPs, thereby demonstrating their minimal cytotoxicity. To further evaluate the cytotoxicity of the hybrid NPs synthesized under different reaction conditions, in vitro cytotoxicity tests were elaborately conducted against B16F10 cells. Figure 8 demonstrates the in vitro cytotoxicity of the core−satellite and dumbbell-like hybrid NPs with different concentrations. Obviously, within the experimental errors, the cell viability was largely unaffected by the presence of the hybrid NPs from 50 to 200 μg/mL. The results indicate that hybrid NPs with the Fe_3O_4 core and Ag nanocrystals protected by the porous carbon shell have good biocompatibility, which is consistent with the previously reported good biocompatibility of the carbon nanomaterials in bioapplications.[68,69]

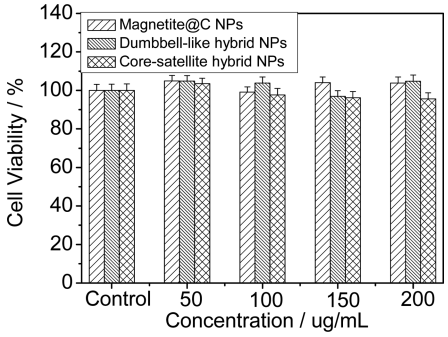

Figure 8. In vitro cytotoxicity of the Fe_3O_4@C−Ag hybrid NPs.

4. CONCLUSIONS

In summary, monodispersed multifunctional Fe_3O_4@C−Ag hybrid NPs containing both magnetite and Ag nanocrystals protected by a porous carbon shell can be synthesized by the first one-step solvothermal synthesis of Fe_3O_4@C template NPs, followed by the loading and in situ reduction of Ag^+ ions in the porous carbon shell in water at room temperature. The nanostructures of the Fe_3O_4@C−Ag hybrid NPs can be readily controlled by varying the reaction concentration of Ag^+ ions. While dumbbell-like structure can be formed at low Ag^+ concentration (e.g, 0.25 mM), the core−satellite structure can be formed at high Ag^+ concentration (e.g., 5 mM). The hydrophilic carboxyl/hydroxyl groups on the carbon surface of the porous carbon shell provide the hybrid NPs excellent dispersibility in water. The hybrid NPs exhibit high catalytic activity for the degradation of Rhodamine B dye molecules in aqueous phase and can be easily recycled for reuse with stable catalytic efficiency. The hybrid NPs can overcome cellular barriers to enter the intracellular region to light up the mouse melanoma B16F10 cells in multicolor modal. More importantly, the hybrid NPs demonstrate no cytotoxicity in the tested concentration range up to 200 μg/mL. The readily prepared Fe_3O_4@C−Ag hybrid NPs that can combine the unique properties and functions of the magnetic Fe_3O_4 core, Ag nanocrystals, and the biocompatible porous carbon shell should find applications in many fields, such as catalysis, drug delivery, magnetic resonance imaging, and optical bioimaging.

■ ASSOCIATED CONTENT

Ⓢ Supporting Information

Figures S1−S10. This information is available free of charge via the Internet at http://pubs.acs.org.

■ AUTHOR INFORMATION

Corresponding Author

*E-mail: shuiqin.zhou@csi.cuny.edu.

Notes

The authors declare no competing financial interest.

■ ACKNOWLEDGMENTS

We gratefully acknowledge the financial support from the PSC−CUNY Research Award (64511-00 42) and American Diabetes Association (Basic Science Award 1-12-BS-243). A portion of this research was conducted at the Center for Nanophase Materials Sciences, which is sponsored at Oak Ridge National Laboratory by the Scientific User Facilities Division, Office of Basic Energy Sciences, U.S. Department of Energy.

■ REFERENCES

(1) Gu, H. W.; Yang, Z. M.; Gao, J. H.; Chang, C. K.; Xu, B. *J. Am. Chem. Soc.* **2005**, *127*, 34−35.
(2) Riedinger, A.; Leal, M. P.; Deka, S. R.; George, C.; Franchini, I. R.; Falqui, A.; Cingolani, R.; Pellegrino, T. *Nano Lett.* **2011**, *11*, 3136−3141.
(3) Hao, R.; Xing, R. J.; Xu, Z. C.; Hou, Y. L.; Gao, S.; Sun, S. H. *Adv. Mater.* **2010**, *22*, 2729−2742.
(4) Wang, C.; Xu, C. J.; Zeng, H.; Sun, S. H. *Adv. Mater.* **2009**, *21*, 3045−3052.
(5) Gao, J. H.; Gu, H. W.; Xu, B. *Acc. Chem. Res.* **2009**, *42*, 1097−1107.
(6) Lu, Y.; Shi, C.; Hu, M. J.; Xu, Y. J.; Yu, L.; Wen, L. P.; Zhao, Y.; Xu, W. P.; Yu, S. H. *Adv. Funct. Mater.* **2010**, *20*, 3701−3706.
(7) Zeng, H.; Sun, S. H. *Adv. Funct. Mater.* **2008**, *18*, 391−400.
(8) Kim, J.; Piao, Y.; Hyeon, T. *Chem. Soc. Rev.* **2009**, *38*, 372−390.
(9) Levin, C. S.; Hofmann, C.; Ali, T. A.; Kelly, A. T.; Morosan, E.; Nordlander, P.; Whitmire, K. H.; Halas, N. J. *ACS Nano* **2009**, *3*, 1379−1388.
(10) Wu, W. T.; Mitra, N.; Yan, E. C. Y.; Zhou, S. Q. *ACS Nano* **2012**, *6*, 4831−4839.

(11) Ma, M.; Chen, H. R.; Chen, Y.; Wang, X.; Chen, F.; Cui, X. Z.; Shi, J. L. *Biomaterials* **2012**, *33*, 989−998.
(12) Wang, H.; Sun, Y.; Yu, Y.; Chen, J.; Li, R.; Cheng, K.; Chen, Q. W. *Dalton. Trans.* **2012**, *41*, 346−350.
(13) Liu, X.; Wang, D.; Li, Y. *Nano Today* **2012**, *7*, 448−466.
(14) Xu, Z.; Hou, Y.; Sun, S. *J. Am. Chem. Soc.* **2007**, *129*, 8698−8699.
(15) Peng, S.; Lei, C.; Ren, Y.; Cook, R. E.; Sun, Y. *Angew. Chem., Int. Ed.* **2011**, *123*, 3158−3163.
(16) Lopes, G.; Vargas, J.M.; Sharma, S. K.; Beron, F.; Pirota, K. R.; Knobel, M.; Rettori, C.; Zysler, R. D. *J. Phys. Chem. C* **2010**, *114*, 10148−10152.
(17) Jiang, J.; Gu, H.; Shao, H.; Derlin, E.; Papaefthymiou, G. C.; Ying, J. Y. *Adv. Mater.* **2008**, *20*, 4403−4407.
(18) Zhang, Y.; Ding, H.; Liu, Y.; Pan, S.; Luo, Y.; Li, G. *J. Mater. Chem.* **2012**, *22*, 10779−10786.
(19) Xu, C.; Sun, S. *Adv. Drug Delivery Rev.* **2013**, *65*, 732−743.
(20) Sonvico, F.; Dubernet, C.; Colombo, P.; Couvreur, P. *Curr. Pharm. Des.* **2005**, *11*, 2095−2105.
(21) Sunderland, C. J.; Steiert, M.; Talmadge, J. E.; Derfus, A. M.; Barry, S. E. *Drug Dev. Res.* **2006**, *67*, 70−93.
(22) Arruebo, M.; Fernández-Pacheco, R.; Ibarra, M. R.; Santamaría, J. *Nano Today* **2007**, *2*, 22−32.
(23) Gupta, A. K.; Gupta, M. *Biomaterials* **2005**, *26*, 3995−4021.
(24) Chi, Y.; Yuan, Q.; Li, Y. J.; Tu, J.; Zhao, L.; Li, N.; Li, X. *J. Colloid Interface Sci.* **2012**, *383*, 96−102.
(25) Ge, J. P.; Zhang, Q.; Zhang, T. R.; Yin, Y. D. *Angew. Chem., Int. Ed.* **2008**, *120*, 9056−9060.
(26) Zhang, X. P.; Jiang, W. Q.; Zhou, Y. F.; Xuan, S. H.; Peng, C.; Zong, L. H.; Gong, X. L. *Nanotechnology* **2011**, *22*, 375701−375707.
(27) Shubayev, V. I.; Pisanic, T. R., II; Jin, S. *Adv. Drug Delivery Rev.* **2009**, *61*, 467−477.
(28) Pan, Y.; Neuss, S.; Leifert, A.; Fischler, M.; Wen, F.; Simon, U.; Schmid, G.; Brandau, W.; Jahnen-Dechent, W. *Small* **2007**, *3*, 1941−1949.
(29) Kawata, K.; Osawa, M.; Okabe, S. *Environ. Sci. Technol.* **2009**, *43*, 6046−6051.
(30) Pisanic, T. R., II; Blackwell, J. D.; Shubayev, V. I.; Finones, R. R.; Jin, S. *Biomaterials* **2007**, *28*, 2572−2581.
(31) Salgueirino-Maceira, V.; Correa-Duarte, M. A. *Adv. Mater.* **2007**, *19*, 4131−4144.
(32) Yoon, T. J.; Yu, K. N.; Kim, E.; Kim, J. S.; Kim, B. G.; Yun, S. H.; Sohn, B. H.; Cho, M. H.; Lee, J. K.; Park, S. B. *Small* **2006**, *2*, 209−215.
(33) Yang, J.; Zhang, F.; Chen, Y.; Qian, S.; Hu, P.; Li, W.; Deng, Y.; Fang, Y.; Han, L.; Luqman, M.; Zhao, D. *Chem. Commun.* **2011**, *47*, 11618−11620.
(34) Lu, Y.; Yin, Y.; Li, Z. Y.; Xia, Y. *Nano Lett.* **2002**, *2*, 785−788.
(35) Liz-Marzan, L. M.; Giersig, M.; Mulvaney, P. *Langmuir* **1996**, *12*, 4329−4325.
(36) Im, S. H.; Herricks, T.; Lee, Y. T.; Xia, Y. *Chem. Phys. Lett.* **2005**, *401*, 19−23.
(37) Ikeda, S.; Ishino, S.; Harada, T.; Okamoto, N.; Sakata, T.; Mori, H.; Kuwabata, S.; Torimoto, T.; Matsumura, M. *Angew. Chem., Int. Ed.* **2006**, *45*, 7063−7066.
(38) Kim, M.; Sohn, K.; Na, H. B.; Hyeon, T. *Nano Lett.* **2002**, *2*, 1383−1387.
(39) Xiao, C.; Chen, S.; Zhang, L.; Zhou, S.; Wu, W. *Chem. Commun.* **2012**, *48*, 11751−11753.
(40) Shokouhimehr, M.; Piao, Y.; Kim, J.; Jang, Y.; Hyeon, T. *Angew. Chem., Int. Ed.* **2007**, *46*, 7039−7043.
(41) Shi, Y. L.; Asefa, T. *Langmuir* **2007**, *23*, 9455−9462.
(42) Lee, J.; Park, J. C.; Song, H. *Adv. Mater.* **2008**, *20*, 1523−1528.
(43) Gu, H.; Zheng, R.; Zhang, X.; Xu, B. *J. Am. Chem. Soc.* **2004**, *126*, 5664−5665.
(44) Wang, D.; Li, Y. *J. Am. Chem. Soc.* **2010**, *132*, 6280−6281.
(45) Xu, Z.; Hou, Y.; Sun, S. *J. Am. Chem. Soc.* **2007**, *132*, 6280−6281.
(46) Pan, Y.; Gao, J.; Zhang, B.; Zhang, X.; Xu, B. *Langmuir* **2010**, *26*, 4184−4187.
(47) Wang, H.; Sun, Y. B.; Chen, Q. W.; Yu, Y. F.; Cheng, K. *Dalton Trans.* **2010**, *39*, 9565−9569.
(48) Wang, H.; Chen, Q. W.; Yu, Y. F.; Cheng, K.; Sun, Y. B. *J. Phys. Chem. C* **2011**, *115*, 11427−11434.
(49) Chughtai, A. R.; Tassim, J. A.; Peterson, J. H.; Stedman, D. H. *Aerosol Sci. Technol.* **1991**, *15*, 112−126.
(50) Smith, D. M.; Chughtai, A. R. *Colloids Surf., A* **1995**, *105*, 47−77.
(51) Duffy, P.; Magno, L. M.; Yadav, R. B.; Roberts, S. K.; Ward, A. D.; Botchway, S. W.; Colavita, P. E.; Quinn, S. J. *J. Mater. Chem.* **2012**, *22*, 432−439.
(52) Socrates, G. *Infrared and Raman characteristic group frequencies. Tables and Charts*; John Wiley & Sons: Chichester, 2001.
(53) Coates, J. Interpretation of Infrared Spectra, A Practical Approach. In *Encyclopedia of Analytical Chemistry*; Meyers, R. A., Ed.; John Wiley & Sons Ltd: Chichester, 2000; pp 10815−10837.
(54) Wiley, B.; Sun, Y.; Xia, Y. *Acc. Chem. Res.* **2007**, *40*, 1067−1076.
(55) Zhang, Q.; Li, W. Y.; Moran, C.; Zeng, J.; Chen, J. Y.; Wen, L. P.; Xia, Y. N. *J. Am. Chem. Soc.* **2010**, *132*, 11372−11378.
(56) Zhang, F.; Wang, C. *J. Phys. Chem. C* **2008**, *112*, 15151−15156.
(57) Jiang, C.; Chen, M.; Xuan, S.; Jiang, W.; Gong, X.; Zhang, Z. *Can. J. Chem.* **2009**, *87*, 502−506.
(58) Kim, M. R; Lee, D. K.; Jang, D. J. *Appl. Catal., B* **2011**, *103*, 253−260.
(59) Tang, S.; Vongehr, S.; Meng, X. *J. Mater. Chem.* **2010**, *20*, 5436−5445.
(60) Amarjargal, A.; Tijing, L. D.; Im, I. T.; Kim, C. S. *Chem. Eng. J.* **2013**, *226*, 243−254.
(61) Liu, P.; Zhao, M. F. *Appl. Surf. Sci.* **2009**, *255*, 3989−3993.
(62) Xie, L.; Chen, M.; Wu, L. M. *J. Polym. Sci., Part A: Polym. Chem.* **2009**, *47*, 4919−4926.
(63) Tang, S.; Vongehr, S.; Meng, X. *J. Phys. Chem. C* **2010**, *114*, 977−982.
(64) Kreibig, U.; Vollmer, M. *Optical Properties of Metal Clusters*; Springer: Berlin, 1995; Vol. 25.
(65) Maretti, L.; Billone, P. S.; Liu, Y.; Scaiano, J. C. *J. Am. Chem. Soc.* **2009**, *131*, 13972−13980.
(66) Zheng, J.; Dickson, R. M. *J. Am. Chem. Soc.* **2002**, *124*, 13982−13983.
(67) Chen, J.; Guo, Z.; Wang, H. B.; Gong, M.; Kong, X. K.; Xia, P.; Chen, Q. W. *Biomaterials* **2013**, *34*, 571−581.
(68) Yang, S.; Wang, X.; Wang, H.; Lu, F.; Luo, P.; Cao, L.; Meziani, M.; Liu, J.; Liu, Y.; Chen, M.; Huang, Y.; Sun, Y. P. *J. Phys. Chem. C* **2009**, *113*, 18110−18114.
(69) Fang, Y.; Guo, S.; Li, D.; Zhu, C.; Ren, W.; Dong, S.; Wang, E. *ACS Nano* **2012**, *6*, 400−409.